Materials Today Bio 14 (2022) 100241

Contents lists available at ScienceDirect

Materials Today Bio

journal homepage: www.journals.elsevier.com/materials-today-bio

# Quantification of doping state of redox sensitive nanoparticles for probing the invasiveness of cancer cells using surface enhanced Raman scattering

Jaehun Lee [a,1], Hwunjae Lee [b,c,d,1], Hyun Jung Kim [a,e], Jongsu Yun [a], Taeha Lee [e,f], Gyudo Lee [e,f], Hyun Soo Kim [g,**], Yoochan Hong [a,*]

[a] Department of Medical Device, Korea Institute of Machinery and Materials (KIMM), Daegu, 42994, Republic of Korea
[b] Department of Radiology, College of Medicine, Yonsei University, Seoul, 03722, Republic of Korea
[c] YUHS-KRIBB Medical Convergence Research Institute, College of Medicine, Yonsei University, Seoul, 03722, Republic of Korea
[d] Graduate Program of Nanoscience and Technology, College of Medicine, Yonsei University, Seoul, 03722, Republic of Korea
[e] Department of Biotechnology and Bioinformatics, Korea University, Sejong, 30019, Republic of Korea
[f] Interdisciplinary Graduate Program for Artificial Intelligence Smart Convergence Technology, Korea University, Sejong, 30019, Republic of Korea
[g] Department of Electronic Engineering, Kwangwoon University, Seoul, 01897, Republic of Korea

ARTICLE INFO

*Keywords:*
Redox activity
Cancer microenvironment
Polyaniline
Silver nanosnowflake
Surface enhanced Raman scattering

ABSTRACT

Redox activity is known to regulate migration, invasion, metastasis, proliferation, and vascularization of cancer. Because cancer is heterogeneous, the role of redox activity in different cancers and cancer-related processes vary widely. In this study, water soluble, Tween 80-coated polyaniline (TPAni) nanoparticles were synthesized and used as nano-agents for sensing the redox activities of various cancer cells. To identify the relationship between the redox activity and the aggressiveness of cancer cells, two different cancer cell lines, derived from the same tissue but different with regards to aggressiveness, were selected for study. First, the cancer cell lines were incubated with TPAni nanoparticles, and an absorbance ratio obtained from the cell culture media was used as a colorimetric indicator of the redox activities of the cells. Simultaneously, hydrophobically modified filter papers coated with silver nanosnowflakes (SNSF) were used as sensing substrates for surface enhanced Raman scattering (SERS). SERS spectra obtained from varying concentrations of rhodamine 6G were used to confirm the detection limit of the SNSF-based SERS substrate. Cell culture media containing TPAni nanoparticles were treated with the SNSF-containing SERS substrates to examine the redox activities of the various cancer cell lines.The redox activities of cancer cell lines were confirmed by absorbance spectral analysis, and these redox activities were better identified via an SERS analysis method. A SNSF-containing SERS substrate, fabricated from SNSF and filter paper, was used to sense redox activity in cancer cell lines and to further identify correlations between redox activity and cancer cell line aggressiveness, as indicated by the use of EpCAM as a biomarker. Finally, potential of *in vivo* redox activity sensing was also confirmed.

## 1. Introduction

Redox activity of cells is an important factor in cell cycle [1], differentiation [2], apoptosis [3], inflammation [4], protein interactions [5], and signaling pathways [6]. Redox activity particularly plays an important part in the regulation of most cell signaling pathways, thereby offering diverse phenotypic probabilities for tumor cells, which in turn allows for the emergence of different cancer characteristics and adaptations to various states in the tumor circumstance [7]. This adaptation makes cancers aggressive diseases, which can coexist with their microenvironments [8]. However, the role of the redox activity in this complex context is poorly understood. Some previously published reports have investigated the redox activity of tumors and the alteration of this activity as a biomarker of tumor progression condition, thereby highlighting the function of redox balance in the beginning and end of the carcinogenesis process [9,10]. Another research suggests that deregulation of redox homeostasis is a hallmark of tumor cells that are progressive and resistant to therapy [11].

* Corresponding author.
** Corresponding author.
*E-mail addresses:* hyunsookim@kw.ac.kr (H.S. Kim), ychong1983@kimm.re.kr (Y. Hong).
[1] These authors contributed equally to this work.

https://doi.org/10.1016/j.mtbio.2022.100241
Received 11 January 2022; Received in revised form 7 March 2022; Accepted 11 March 2022
Available online 12 March 2022

To sense the redox activity of biological system, various materials have been used. For example, naphthoquinone, which contains a quinone moiety and undergoes reversible $2e^{-}$, $2H^{+}$ redox reactions, has been used [12]. In addition, mercaptobenzoic acid has been applied to detect redox potential and intracellular pH [13]. More recently, polyaniline (PAni), a conductive polymer, has been utilized to measure the redox activity of biological systems. PAni-based nanostructures are widely used as sensor materials because of their easy synthesis, low price per monomer, adjustability of optoelectronic characteristics, and good chemical stability compared to other conjugated polymers. In particular, PAni has a specific property that can change electrical and optical characteristics depending on doping states by various dopants such as strong acids, Lewis acids, transition metals, and alkali ions. Therefore, the use of PAni nanoparticles has the advantage of not only detecting specific molecules, but also confirming the overall redox activity of a specific system. For example, water soluble PAni nanoparticles have been used as colorimetric nanoprobes to identify redox activity of live, fixed, and lysed cancer cells [14]. Moreover, PAni has been used as a part of nanocomposites, functioning as a contrast agent for magnetic resonance imaging (MRI) as well as a nanoprobe for redox sensing, *in vitro* and *in vivo* [15]. In addition, in combination with hyaluronic acid, PAni has been used as an active coloring probe to sense cancer redox microenvironments [16]. Furthermore, PAni can establish various composites with other organic or inorganic materials and is employed in a number of applications. PAni-Au nanocomposites have been applied as the labelling agent for highly efficient electrochemical immunoassay [17], glucose sensing by non-enzymatic principle using reduced graphene oxide with PAni and nickel [18], and a framework of graphene oxide with PAni nanowires have been utilized as a biosensing platform for detecting kanamycin based on gas pressure [19]. Regarding research based on the perspective of the cancer microenvironment and materials, recently, studies to treat cancer after controlling the cancer microenvironment using various materials are also being conducted. Surface-oxidized arsenene nanosheets ($As/As_xO_y$ NSs) can produce reactive oxygen species and consume glutathione for cancer therapy [20]. Vermiculite, a clay material, was made into a sandwich structure and used for cancer theranostics [21]. Zinc (II) phthalocyanine-based hybrid nanobullets, which is only composed of organic materials have been used as a synergistic photothermal therapeutic and thermodynamic therapeutic agent for hypoxic cancer with oxygen independent way [22].

Besides material-based approaches towards sensing redox activity, as described earlier, methodological-based approaches have also been used in sensing the redox activity of biological systems. Among these methods, the most commonly used one is fluorescence spectrometry, and the ratiometric fluorescence method has been applied to monitor the action of redox-directed cancer therapeutics [23]. In recent years, Raman spectroscopic methods have emerged and used to sense the redox activity of biological systems due to their capability of chemical structure analysis. For example, Raman technique has been used to sense the intracellular and extracellular pH [24], as well as intracellular redox potential in cancer cells [25]. Moreover, Raman technique was used to determine the redox states of flavin mononucleotide [26], apply to *in situ* nanoscale redox mapping via tip-enhanced Raman spectroscopic method [27], and monitor the redox state of cytochrome *c* in yeast cells during cell death [28]. However, even if redox activity could be measured in various ways, no research has not been reported yet that can directly correlate the cancer aggressiveness using Raman analysis directly related to cancer aggressiveness using Raman analysis.

In this research, Tween 80-coated PAni (TPAni) nanoparticles were synthesized using a solvent-shift method and utilized as nanoprobes in sensing the redox activity of various cancer cells. Absorbance and Raman signal of PAni depend on the doping state (Fig. 1a); therefore, the redox

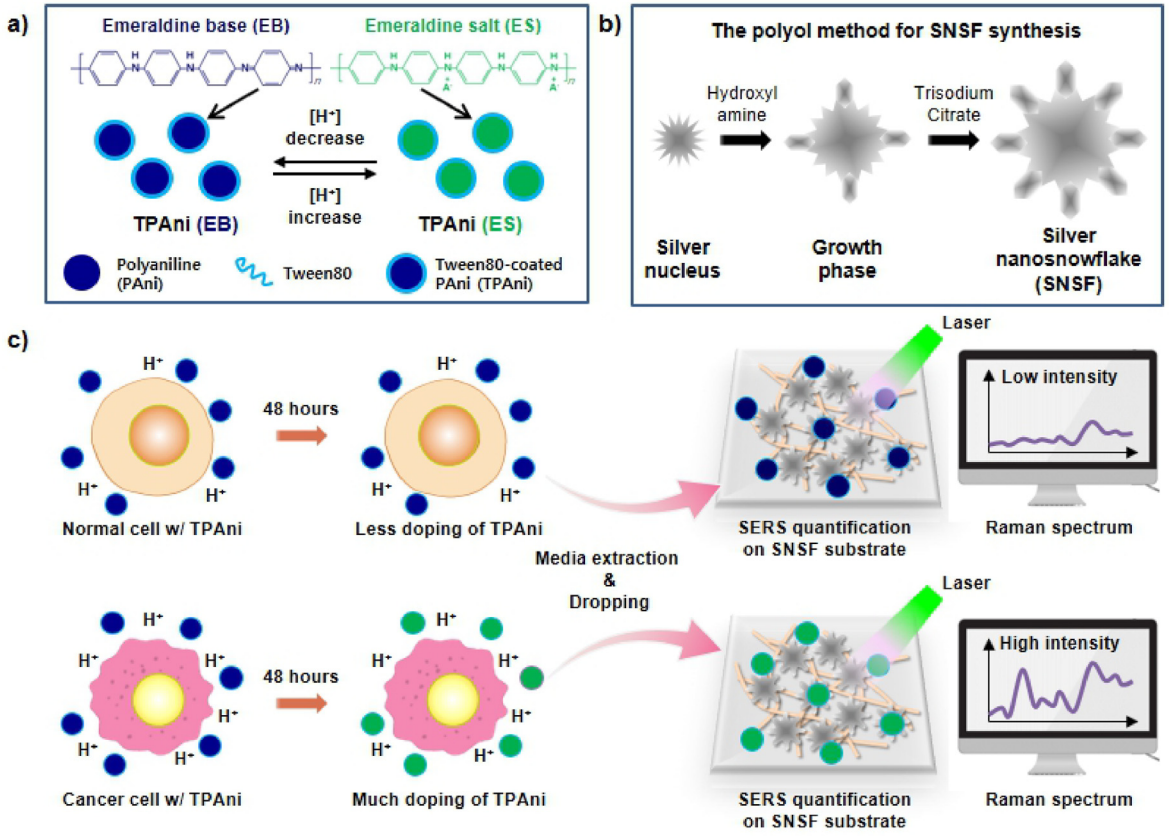


**Fig. 1.** Schematic illustrations of (a) conversion of TPAni nanoparticles according to surrounding environment, (b) synthetic process of SNSF nanoparticles, (c) determination of aggressiveness of cancer cells using a combination of TPAni nanoparticles and Raman spectra.

activity of various cancer cell lines was determined by calculation of an absorbance ratio and Raman intensity ratio. Subsequently, the calculated redox activity for each cancer cell line was compared with the expression level of cancer metastasis-related biomarkers. In particular, to more accurately measure the redox activity for each cancer cell line, TPAni nanoparticles incubated with cancer cells were treated onto a paper-based silver nanosnowflake (SNSF) (Fig. 1b)-containing surface enhanced Raman scattering (SERS) substrate to measure the SERS signals (Fig. 1c). SNSF was selected as a plasmonic material because it enhances the Raman signals due to its morphological property, and precise measurement is also possible due to its characteristic of silver material. Raman signals from TPAni nanoparticles attached onto SNSF substrate were then analyzed to calculate the redox activity of cancer cell lines, and these results were compared to the determined absorbance ratio. The results presented here provide insight into researches focusing on redox activity caused by the microenvironment of cancer cells. In recent years, various researches to examine the redox states in cancer cells have been carried out. Particularly, many studies have been conducted to detect reactive nitrogen species or reactive oxygen species using fluorescent ratiometric sensors [29,30], a chemiluminescence sensor [31], and electrochemical sensors [32,33]. However, the fluorescent ratiometric sensors have many difficulties that are likely to be hampered by other environmental changes or quenching conditions, and the chemiluminescence sensors are limited in relative low analytical accuracy, signal drift phenomenon, and short life time. In addition, the performance of the electrochemical- based sensors are determined by the structures or characteristics of electrode materials such as sensitivity, selectivity, and stability. Compared to aforementioned sensing techniques, the combination of TPAni nanoparticles and SNSF-based SERS substrates have advantages of improved (or higher) sensitivity, accuracy, and rapidity. Furthermore, because TPAni nanoparticles are composed of only organic materials, TPAni nanoparticles improved biocompatibility compared to metal based nanoparticles (e.g., gold or silver).

## 2. Materials and methods

### 2.1. Materials

Polyaniline (PAni) MW~5,000, Tween 80, 1-Methyl-2-Pyrrolidone (NMP), silver nitrate ($AgNO_3$), hydroxylamine solution (HA, 50 w/w in water), and trisodium citrate were purchased from Sigma-Aldrich Chemical Co (USA). Alkyl ketene dimer (AKD) was obtained from Solenis (Gimcheon, Korea). The grade 5C filter papers were obtained from Advantec (USA). In all synthetic processes, ultrapure deionized (DI) water was used. All other chemicals and reagents utilized in the experiments were analytical grade.

### 2.2. Preparation and characterization of Tween 80-coated polyaniline (TPAni) nanoparticles

TPAni nanoparticles were synthesized using a previously reported method with few modifications [14]. First, 100 mg of Tween 80 was dissolved in 30 mL of DI water, and 4 mL of NMP containing 5 mg of PAni polymer was added to a DI water solution containing Tween 80. The solution was stirred at room temperature for 4 h. And then, TPAni nanoparticles were centrifuged using centrifuge tubes with centricon filter (MWCO: 3000 Da). The resultant solution was re-dispersed in DI water, and mass concentration of PAni was adjusted to 1 mg/mL by adding DI water.

### 2.3. Atomic force microscopic (AFM) imaging of TPAni nanoparticles

Atomic force microscopy (AFM, MultiMode 8-HR, Bruker, USA) was used to characterize the morphology of the TPAni nanoparticles. To absorb TPAni nanoparticles onto AFM Mica Discs (diameter: 12 mm) (Ted Pella, USA), a 5 μL aliquot of 1 mg/mL TPAni nanoparticles was deposited onto freshly cleaned mica plates for 15 min, which were then washed with DI water and dried under nitrogen. AFM imaging was carried out at 23 °C in contact mode using 127 μm long cantilevers (TESP-V2, BRUKER, USA) with a resonance frequency of 290–310 kHz.

### 2.4. Cancer cell incubation with TPAni nanoparticles

Cancer cells that originated from 3 different organs; breast (MDA-MB-231, MCF-7), liver (Huh-7, SK-HEP-1), and lung (A549, H23), were used to evaluate the performance of the TPAni nanoparticles. All cell lines were cultured with advanced DMEM/F12 (Thermo-Scientific, USA), 10% FBS, 1% Penicillin-Streptomycin, and 1% L-glutamine and sub-cultured every 3 days. When the cells reached 80% confluence in T-75 flasks, the culture medium was removed, and the flasks were washed with 5 mL of 1× DPBS (Thermo-Scientific). The cells were detached from the flask via treatment with 2 mL of 0.25% trypsin EDTA solution and incubation at 37 °C, 5% $CO_2$ for 3 min. Then, 2 mL of advanced DMEM/F12 with 10% FBS were added to the flask to inactivate trypsin. The cell suspensions were collected from the flasks, centrifugated at 400 g for 3 min, and re-suspended with fresh advanced DMEM/F12 medium. The cancer cells were seeded into 24 well micro-plates at a concentration of $5 \times 10^4$ cells/mL (at least 3 replicas for each experimental condition) and incubated at 37 °C, 5% $CO_2$ to facilitate attachment. After 24 h, the cell medium was removed and fresh medium containing 1% TPAni nanoparticles (1 mg/mL) was added. Following incubation of the cells at 37 °C, 5% $CO_2$ for additional 24 h, 1.5 mL of the supernatant was collected from each culture well for absorbance and Raman spectra analysis. All cells were distributed from Korea Cell Line Bank.

### 2.5. Synthesis and characterization of silver nanosnowflakes (SNSF)

Colloidal suspensions of SNSF were synthesized using the polyol method, as described within a previously published report with some modifications [34]. HA (500 μL, 60 mM) was added into 500 μL of NaOH (50 mM). Subsequently, 9 mL of $AgNO_3$ was added into the mixture at a flow rate of 1 mL/min using syringe pump, and the solution was stirred for 5 min at 500 rpm. After the reaction, 100 μL of trisodium citrate (1% w/v) were added to the mixture and stirring was continued for 15 min at 500 rpm. The resultant solution was centrifuged using a Centricon filter (MW cutoff: 3000 Da) for 1 h at 2000 rpm, and the SNSF were finally dispersed in 10 mL of DI water.

### 2.6. Fabrication of filter paper-based SNSF Raman substrate

The sensitive filter paper-based SNSF substrates were fabricated by following a protocol described in a previously published report with some modifications [35]. The filter paper was cut to a diameter of 5 mm with a punch, and the filter paper fragments were immersed in 0.01% v/v of AKD solution for 5 min. Following AKD treatment, the filter paper was washed totally with DI water and dried at 70 °C for 1 h.

### 2.7. Raman signal measurements

Raman spectra were acquired using a protocol described in a previously published report with some modifications [36]. The Raman spectra were obtained using a 785-nm laser by a hand-held Raman spectrometer (Nanoscope Systems, Inc., NS-100, Daejeon, Korea). The laser power was set as 80 mW, the maximum power of used las. While measuring the Raman spectra, the space between samples and the spectrometer was maintained constantly while Raman spectra acquisitions to keep the laser beam size for one mm on the SNSF substrates. The integration time was kept to 10.0 s. For Raman spectra analysis of samples on the SNSF

substrate, spectra were measured and collected at 10 different positions for each substrate with identical measurement conditions, such as laser power, integration time, distance between sample and spectrometer, and spot location) for statistical analysis.

### 2.8. Analysis of EpCAM expression levels

EpCAM specific immuno-fluorescence staining was conducted to confirm EpCAM expression levels by the six different cancer cell lines (Breast: MCF-7 and MDA-MB-231, Liver: Huh-7 and SK-HEP-1, and Lung: A549 and H23). The cell lines were cultured with advanced DMEM/F12 (Gibco™, USA) containing 10% v/v FBS (Gibco™), 1% L-glutamine (Gibco™), and 1% penicillin/streptomycin (Gibco™) at 37 °C, 5% $CO_2$. The cells were subcultured every 3 days. For immuno-staining, the cell lines were fixed with 4% formaldehyde solution (Sigma-Aldrich) for 15 min at room temperature. After fixation, the cells were washed with 1× DPBS (Gibco™) three times. The cell lines were resuspended in 1× DPBS at $10^6$ cells/mL concentration with final volume of 1 mL. FITC labeled EpCAM antibody (20 μL; BD Biosciences, cat#347197, USA) was reacted with each cell solution for 1 h at 4 °C. Subsequently, the cells were washed with 1× DPBS three times. Fluorescence by the immuno-stained cells was measured using an IX73 fluorescence microscopic system (Olympus, Japan) and analyzed by ImageJ image processing program (NIH, USA). To account for cell size variation, fluorescence densities (A.U) were divided by the unit area ($\mu m^2$).

### 2.9. MCF-7 and MDA-MB-231 animal models

All animal experiments were conducted with the approval of the Association for Assessment and Accreditation of Laboratory Animal Care International. To establish the orthotopic mouse model of breast cancer, MCF-7 and MDA-MB-231 cells ($5.0 \times 10^6$ cells) were implanted into female mice (6-week-old BALB/c-nude mice). When tumor size reached approximately 500 $mm^3$ (tumor volume in $mm^3$ is calculated by following formula, tumor volume = $4/3 \times \pi \times$ (width/2) × (length/2) (heighr/2)), the tumors were extracted.

## 3. Results and discussion

### 3.1. Size and uniformity of synthesized TPAni nanoparticles

TPAni nanoparticles were synthesized by applying some modifications to the solvent-shift method used in the previously published study [14]. After synthesis of TPAni nanoparticles, TPAni nanoparticle morphology was confirmed via atomic force microscopy (AFM) imaging (Fig. 2a). As shown in Fig. 2a, TPAni nanoparticles exhibited a spherical morphology. As additional confirmation of TPAni nanoparticle morphology, 3D images of single TPAni nanoparticle that are denoted in Fig. 2a were analyzed as shown in Fig. 2b. The average height of the four individual TPAni nanoparticles was 40.29 ± 6.38 nm, and the average width was 140.63 ± 9.02 nm (Fig. 2c). For statistical analysis, the heights of 50 single TPAni nanoparticles were analyzed, and the resultant histogram showed that the average size of TPAni nanoparticles was 36.18 ± 7.64 nm (Fig. 2d). The chemical structure of TPAni nanoparticles was confirmed by Fourier transform infrared (FT-IR) spectral analysis (Fig. S1). FT-IR spectra obtained from the TPAni nanoparticles showed peaks at 1,330, 1,467, and 1,563 $cm^{-1}$ that were occurred due to aromatic C–N stretching, C═C/C═N stretching of benzenoid rings, and C═C/C═N stretching of the quinoid rings of PAni, respectively. A peak at 1,740 $cm^{-1}$ corresponds to C═O bonding from the ester group of Tween 80. In addition, X-ray photoelectron spectroscopic (XPS) analysis of the TPAni nanoparticles was conducted (Fig. S2). C1 core level XPS spectra were de-convoluted into three peaks that corresponds to C═O/C–O, C═N+/C–Cl, and C–C/C–H at 286.7 eV, 285.8 eV, and 284.4 eV, respectively. Deconvolution of the asymmetric N1s peak observed at 400.0 eV yielded three peaks; specifically, peaks correspond to a quinoid phenyl structure (-N = ), a benzenoid structure (–NH–), and a quaternary ammonium structure (N+) at 398.7, 400.0, and 401.7 eV, respectively. Likewise, O1s peaks were de-convoluted into two bands with binding energies. The O1s curve at 532.7 was generated by a combination of the backbone $–CH_2$-*O*-$CH_2$ and the oxygen in the carboxyl group (-C═O-) of Tween 80 that interacted with surface of the PAni (532.1 eV). The XPS analyses presented here-in was consistent with previously published research on XPS analysis of PAni and Tween 80 [37, 38]. From Fig. 2, TPAni nanoparticles were confirmed to be small and stable.

### 3.2. pH response of TPAni nanoparticles as redox sensitive nanoparticles

To investigate the potential of TPAni nanoparticles as optical nanoprobes for sensing the redox activity of cancer cells, color changes of TPAni nanoparticles were characterized by varying pH values. As seen in Fig. 3a, TPAni nanoparticles exhibited an active coloring effect due to protonation. At low pH values (< pH 2), the chemical structure of TPAni nanoparticles transitioned from an emeraldine base (EB) to an emeraldine salt (ES) state (green color), while relatively high pH values (> pH 2), the chemical structure of TPAni nanoparticles transitioned from the ES to the EB state (blue color). Variation in absorbance spectra of TPAni nanoparticles according to pH value is shown in Fig. 3b. The Raman signals of TPAni nanoparticles in each pH value were also acquired to investigate the sensing capability of the developed technique for analyzing the redox activity of cancer cell lines (Fig. 3c). Analysis of Raman spectra from the doping state of TPAni nanoparticles showed peaks corresponding to quinoid ring deformation at 747 and 833 $cm^{-1}$,

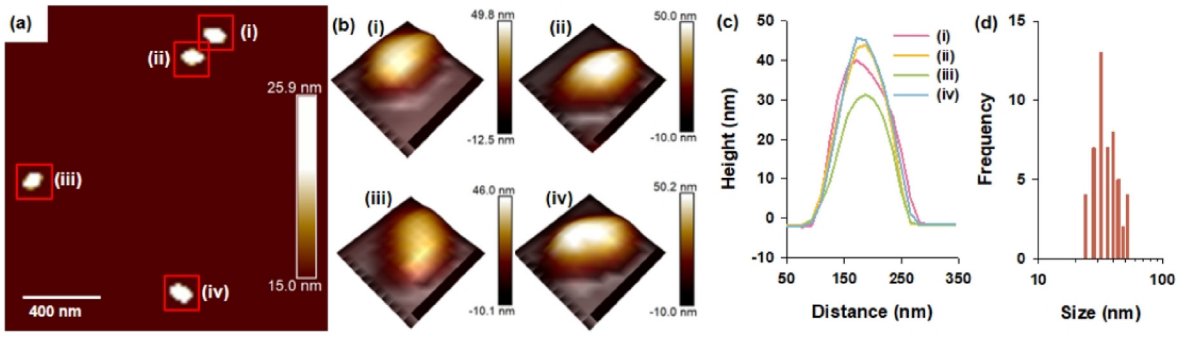


**Fig. 2.** (a) An AFM image of TPAni nanoparticles. (b) 3D-AFM images of four individual single TPAni nanoparticle, and (c) height profiles of TPAni nanoparticles denoted in (a). (d) Size distribution of TPAni nanoparticles ($n = 50$).

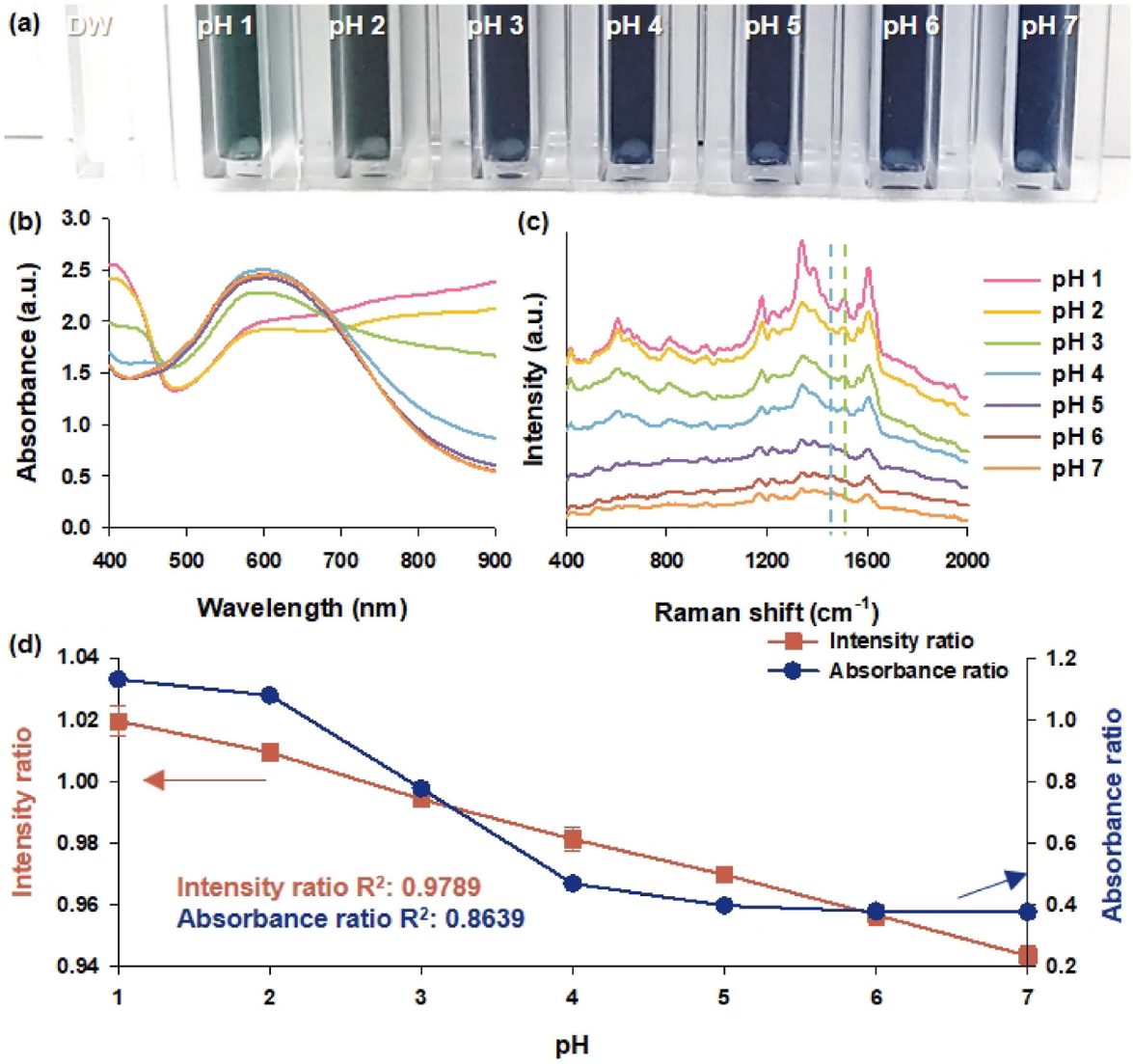


**Fig. 3.** (a) A photograph, (b) absorbance spectra, (c) Raman spectra, and (d) absorbance and Raman intensity ratios of TPAni nanoparticles as varying the surrounding pH values.

C–H bending in the quinoid ring at 1164 $cm^{-1}$, and C═N stretching quinoid ring at 1457 $cm^{-1}$. In contrast, the ES state showed peaks that corresponded to radical cation by protonation at 1336 $cm^{-1}$ and *N*–H bending at 1509 $cm^{-1}$ (Table S1). To quantify the chemical and doping state (i.e., the EB (dedoped) and ES (doped) states of TPAni nanoparticles), absorbance ratio ($A_{900}/A_{600}$) was calculated from the absorbance values at characteristic wavelengths of the peak position for EB ($A_{600}$) and ES ($A_{900}$) (Fig. 3d). TPAni nanoparticles did not precipitate or aggregate during experiments designed to evaluate changes in absorbance properties that occurred with changes to the surrounding pH (Fig. 3a–d). At pH 1, TPAni nanoparticles existed in the ES (doped) state, as indicated by the existence of polaron bands transitions and π-π* transitions of the benzenoid rings at about 400 and 800–1000 nm, respectively. From the increment of the pH, the polaron bands corresponds to 400 and 800–1000 nm gradually decreased in absorbance spectra, and a strong absorbance peak at about 600 nm was observed. The latter peak resulted from excitation from the highest occupied molecular orbital (HOMO) of the three ring benzenoid part of the system to the lowest unoccupied molecular orbital (LUMO) of the localized quinoid ring and the two surrounding imine nitrogens in the EB state of the TPAni nanoparticles [39]. Thus, by pH increment from pH 1 to pH 5, the absorbance ratio ($A_{900}/A_{600}$) decreased dramatically; however, additional changes in the absorbance ratio did not occur at higher pH values (> pH 5). In addition, a Raman intensity ratio ($I_{ES}/I_{EB}$) was also calculated from representative peaks for the EB (dedoped) and ES (doped) states. Representative peaks were selected as indicators of the transition of the doped state of TPAni nanoparticles upon exposure to various pH values. The peak at 1457 $cm^{-1}$ was used as an indicator of the EB state of TPAni nanoparticles, while the peak 1509 $cm^{-1}$ was used as an indicator of the ES state. Compared to the variation in the absorbance ratio with the pH values, the variation in the Raman intensity ratio as a function of pH values was more linear. The reason why Raman intensity ratio came out more linear is thought to be because the Raman intensity ratio detects meaningful changes in the chemical structure of TPAni nanoparticles more accurately. From the results for Fig. 3, the redox sensing capability of TPAni nanoparticles can be more accurately measured through Raman analysis.

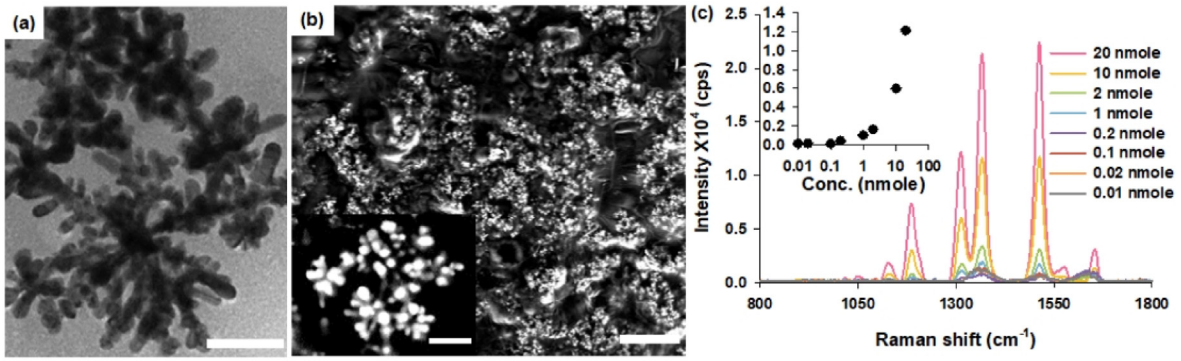


**Fig. 4.** a) A FE-TEM image of SNS nanoparticles. Scale bar represents 200 nm. b) FE-SEM image of SNSF nanoparticles-coated hydrophobic filter paper. Scale bar represents 2.5 μm. An inset is magnified image of SNSF nanoparticles on hydrophobic filter paper. Scale bar is 400 nm. c) SERS spectra of R6G dropped onto SNSF adsorbed paper substrate as varying the concentrations. The inset is intensity at 1511 cm$^{-1}$ according to concentration of R6G.

### 3.3. Characterization of SNSF-based SERS substrate

To more precisely correlate the redox activity with the aggressiveness of the cancer cells, a SERS substrate was manufactured to include SNSF. As shown in Fig. 4a, the SNSF were characterized by the presence of seven to twelve arms that radiate from the core. In characterizing the SNSF substrate, the average size of SNSF was measured to be 300–400 nm, and the number of arms in the SNSF were found to vary from an average arm number of eight. As shown in Fig. 4a, some of these arms were branched, and the tips of the arms were generally not sharp. Fig. S3 provides the spatial distribution of silver within the SNSF through energy dispersive X-ray elemental mapping images, while Fig. S4 shows the absorbance spectrum of colloidal SNSF suspensions. SNSF were entirely composed of silver (Fig. S3); and, as shown in Fig. S4, SNSF gave rise to a strong peak at 386 nm, because of bulk plasmon resonances, and an absorbance background at longer wavelength with a weak maximum at 875 nm. The high absorbance background is due to the scattering emission and absorption generated by SNSF with varying morphologies. This variation in shape led to differences in localized surface plasmon resonances in the aqueous dispersion, covering a wide range of wavelengths from the visible to near infrared regions. The hydrophobicity of the filter paper surface on the SERS substrate was enhanced through an esterification reaction between an alkyl ketene dimer (AKD) solution and the hydroxyl groups expressed on cellulose fibers that is components of filter paper. As verification of hydrophobically modification, the contact angle of an aqueous sample droplet on the hydrophobic filter paper by esterification reaction using AKD was determined to be 125.3°±5.0° (Fig. S5), and the droplet of aqueous sample was maintained on the surface of the hydrophobic filter paper for an hour until dry. The cellulose fibers were functionalized via AKD treatment to increase the hydrophobicity of filter paper. The intention of the hydrophobic treatment is to avoid the fast soaking of samples to the filter paper, enabling the aqueous samples to be maintained as a droplet form on the surface of filter paper. The process can provide more SNSF nanoparticles to exist in localized area onto the surface of filter paper, which can be superior to generation of hot-spot for SERS and enable more sample analytes to exist on the surface of SERS-active area. Consequently, aqueous solutions of SNSF and TPAni nanoparticles were maintained within a localized small area on the hydrophobic surface of the filter paper for a long time. As indicated in Fig. 4b, SNSF distribution on the filter paper with hydrophobic modification was evaluated by field emission-scanning electron microscopic (FE-SEM) imaging. As shown during FE-SEM image analysis, the SNSF was accumulated in the form multi-layered SNSF stacked structures, with larger than several micro-meter sizes, onto the surface of the hydrophobic treated filter paper. To confirm the possibility of the SNSF-containing substrates as SERS substrates, the Raman spectra from rhodamine 6G (R6G) at various concentrations were obtained, and the intensities of a representative peak at 1511 cm$^{-1}$ were plotted according to the known molecules numbers (moles) of R6G (Fig. 4c). Based upon experiments to assess the capability of SNSF substrate as a SERS substrate using R6G, the highest peak of R6G was confirmed at 1509 cm$^{-1}$ because of the aromatic C–C stretching vibrations. The other peaks identified within the Raman spectra corresponded to C–C–C ring in plane bending vibrations at 614 cm$^{-1}$, C–H out of plane bending vibrations at 772 cm$^{-1}$, and C–H in plane bending vibrations at 1129 cm$^{-1}$, and aromatic C–C stretching vibrations at 1,311, 1,360, and 1651 cm$^{-1}$. From the Fig. 4, SNSF nanoparticles were successfully synthesized and SNSF attached filter paper based substrate can be used as a SERS substrate.

### 3.4. Redox sensitive nanoparticles based SERS analysis of cell media from various cancer cell lines

Before treatment of TPAni nanoparticles to cancer cell lines, the absorbance ratios were calculated according to the PAni concentration by chemical states (EB and ES) of TPAni nanoparticles. As shown in Fig. S6, it was confirmed that absorbance ratios remained almost constant for each chemical state, and these values matched the range of absorbance ratio in Fig. 3d. These results show that even if the cellular uptake of TPAni nanoparticles occurs and the concentration of TPAni nanoparticles in the solution changes, the absorbance ratio remains constant. Similar to the absorbance ratio, we think that Raman intensity ratio will be constant for each cell line without any changes for nanoparticles concentration. In addition, TPAni nanoparticles were treated on SNSF substrate for each chemical state (EB and ES), and then SERS spectra of TPAni nanoparticles were measured (Fig. S7). As described in Fig. 3c, peaks of PAni shown in Table S1 were also identified on the SNSF substrate. The cell viability of cancer cell lines under the treatment of TPAni nanoparticles were evaluated before conducting cell-based experiments (Fig. S8). The cell viability of 75% or higher was confirmed at the concentration of TPAni nanoparticles of 0.01 mg/mL for all cell lines, and subsequent experiments using cells were conducted by administering a concentration of TPAni nanoparticles of 0.01 mg/mL.

Cancer cell lines were treated and incubated with TPAni nanoparticles, and the supernatants were collected to measure Raman signals using the SNSF substrates. Raman spectra of breast, liver, and lung-derived cancer cell lines are shown in Fig. 5a–c. Two cancer cell lines with same origin (breast, liver, and lung) of different aggressiveness were grouped. Fig. 5d–f shows that cancer cell lines with relatively low aggressiveness have a lower Raman intensity ratio than cancer cell lines with relatively high aggressiveness. In particular, in the case of H-23

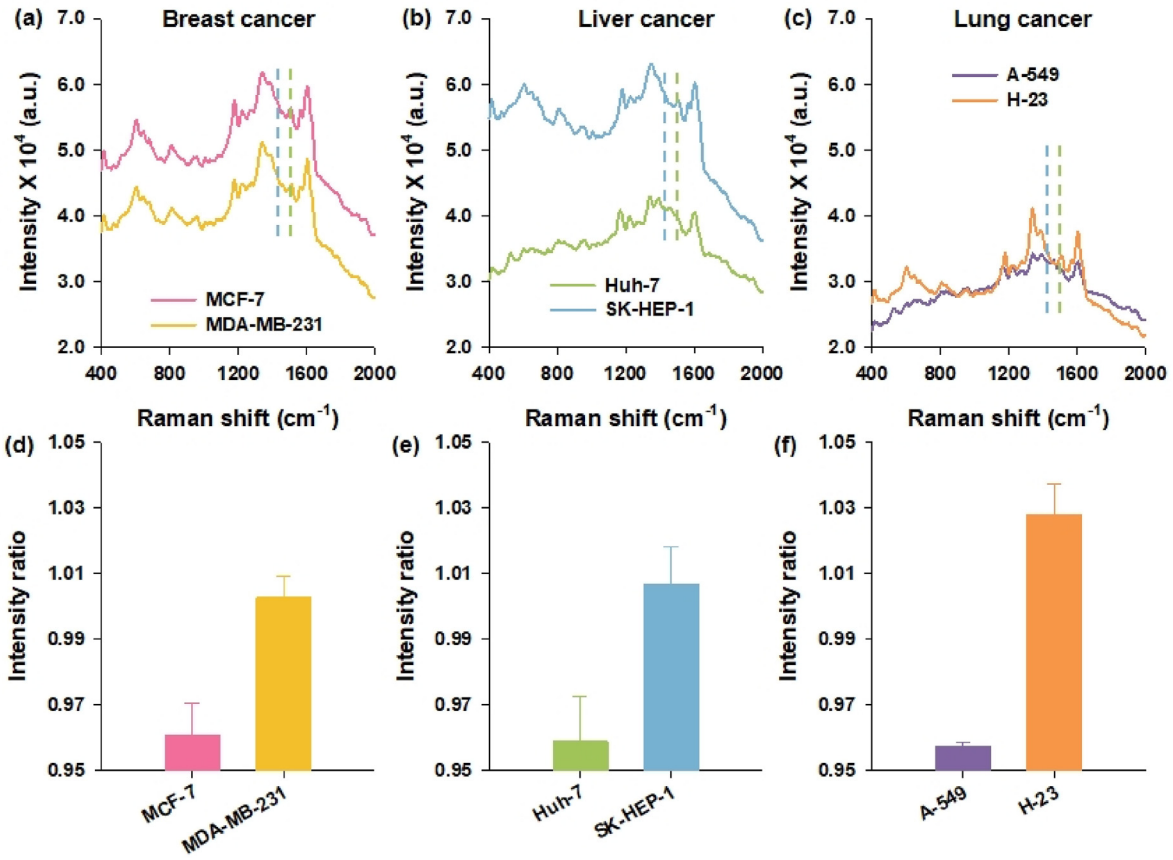


**Fig. 5.** Raman spectra for a) breast cancer cell lines, b) liver cancer cell lines, and c) lung cancer cell lines classified according to the origin of cancer. The dotted lines represent EB (1457 $cm^{-1}$, blue) and ES (1509 $cm^{-1}$, green) specific Raman shift, respectively. Raman intensity ratios for d) breast cancer cell lines, e) liver cancer cell lines, and f) lung cancer cell lines classified according to the origin of cancer.

cells, which are lung cancer cell lines, the Raman intensity ratio value was calculated as 1.0285 and showed the highest value among cancer samples tested. In addition, absorbance spectra were obtained and absorbance ratios ($A_{900}/A_{600}$) were also calculated for cancer cell lines that originated from three different organs (breast, liver, lung) ($A_{900}/A_{600}$) to sense redox activity (Figs. S9a and b). The color of the supernatants obtained from each culture medium was turquoise, and the corresponding absorbance spectra are shown in Fig. S9a. Moreover, in experiments using cancer cell lines, the absorbance ratios ($A_{900}/A_{600}$) did not exceed 0.4, a value that corresponded to a pH of 5 or more in Fig. 3d. When comparing highly aggressive to less aggressive cancer cells (MDA-MB-231 and MCF-7 for breast cancer, SK-HEP-1 and Huh-7 for liver cancer, and H-23 and A-549 for lung cancer), highly aggressive cancer cell lines had relatively higher absorbance ratios ($A_{900}/A_{600}$) (Fig. S9b).

### 3.5. Fluorescence analysis and correlation with SERS signal

In order to determine the correlation between redox activity and aggressiveness for each cancer cell line, epithelial cell adhesion molecule (EpCAM) protein was selected as a biomarker for evaluating the aggressiveness in cancer cells, and the EpCAM expression levels were measured through fluorescence microscopic analysis (Fig. 6a). The fluorescence intensity per unit area was determined (Fig. 6b), and the reciprocal of fluorescence density per unit area was compared to Raman intensity ratio for each cell line (Fig. 6c). After obtaining Raman signals from TPAni nanoparticles incubated with cancer cell lines and calculating the Raman intensity ratio ($I_{ES}/I_{EB}$) (Fig. 5d and e), the expression level of a cancer aggressiveness-related biomarker for each cancer line was determined for correlation with the Raman intensity ratio. EpCAM protein was selected as an aggressiveness-related biomarker due to an association with cell adhesion and migration. As more EpCAM proteins are expressed, the better the cells become adhered, and the less aggressive the cells become; in contrast, as less EpCAM proteins are expressed and cells become less adhered, the more aggressive the cells become. Comparing the results of EpCAM expression levels to the calculated Raman intensity ratios, the values were found to be well matched ($R^2 = 0.9752$). In contrast, a relatively low $R^2$ value ($R^2 = 0.0995$) was derived from the correlation graph between the absorbance ratio and fluorescence (Fig. S9c). During the metabolism in cancer cells, the redox stress caused by the Warburg effect elevates the concentration of metabolites such as lactate, pyruvate, and co-enzymes, which can perform as biodopants [40]. Of all the cancer cell metabolites, elevated lactate by the Warburg effect influences cancer metastasis, aggressiveness, migration, and prognosis in numerous cancer cells. According to more recent studies, the Warburg effect down-regulates the mitochondrial activity, and this down-regulation prevents an over production of adenosine triphosphate (ATP) and $CO_2$. The loss of ATP and $CO_2$ is related with the enhanced activities of membrane pumps favoring an intracellular alkaline pH and an extracellular acidity [41]. This redox activity functions as a driving force in many aspects of metastasis and aggressiveness in cancer cells [42]. Collectively, the Raman signal measurements and the calculation of Raman intensity ratios using a combination of TPAni nanoparticles and SERS were able to sense redox activity of cancer cell lines more precisely than what was previously observed from the absorbance analysis method alone. Furthermore, the calculated Raman intensity ratio was consistent with aggressiveness-related biomarker expression level for cancer cell lines.

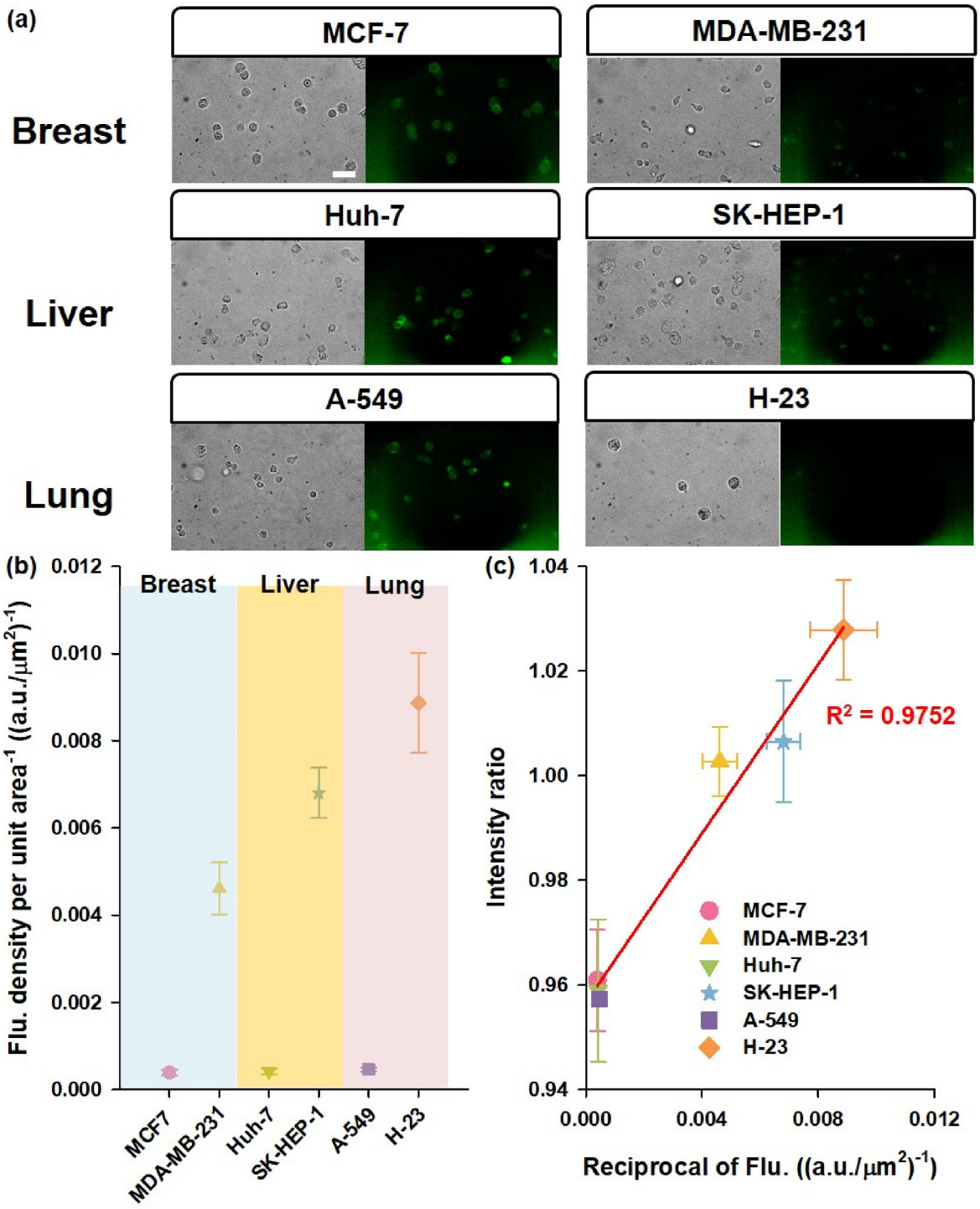


**Fig. 6.** a) Bright field microscopic images (left column) and fluorescence images incubated with FITC functionalized *anti*-EpCAM antibody (right column). A scale bar is 40 μm. b) The reciprocal of fluorescence density per unit area for indicated cancer cell lines. Additional boxes are origins of each cancer cell line. c) Raman intensity ratios between reciprocal of fluorescence density per unit area of TPAni nanoparticles incubated with indicated cancer cell lines.

### *3.6. SERS signal measurements from lysed samples obtained from animal model*

To confirm the potential of combination of TPAni nanoparticles and SNSF substrate for sensing redox activity of cancer *in vivo*, lysed breast cancer tissue samples extracted from MCF-7 and MDA-MB-231 mouse models (Fig. 7a and b) were incubated with TPAni nanoparticles. Following the incubation, TPAni nanoparticles with lysed tissue samples were treated onto SNSF substrate. Raman spectra of TPAni nanoparticles with each cancer tissue are shown in Fig. 7c. Raman intensity ratios were also calculated for each Raman spectrum (Fig. 7d). In the case of *in vivo* experiments, compared with Fig. 5d, the Raman intensity ratios were slightly lower, however, it is judged that potential of detecting *in vivo* redox activity was sufficiently confirmed.

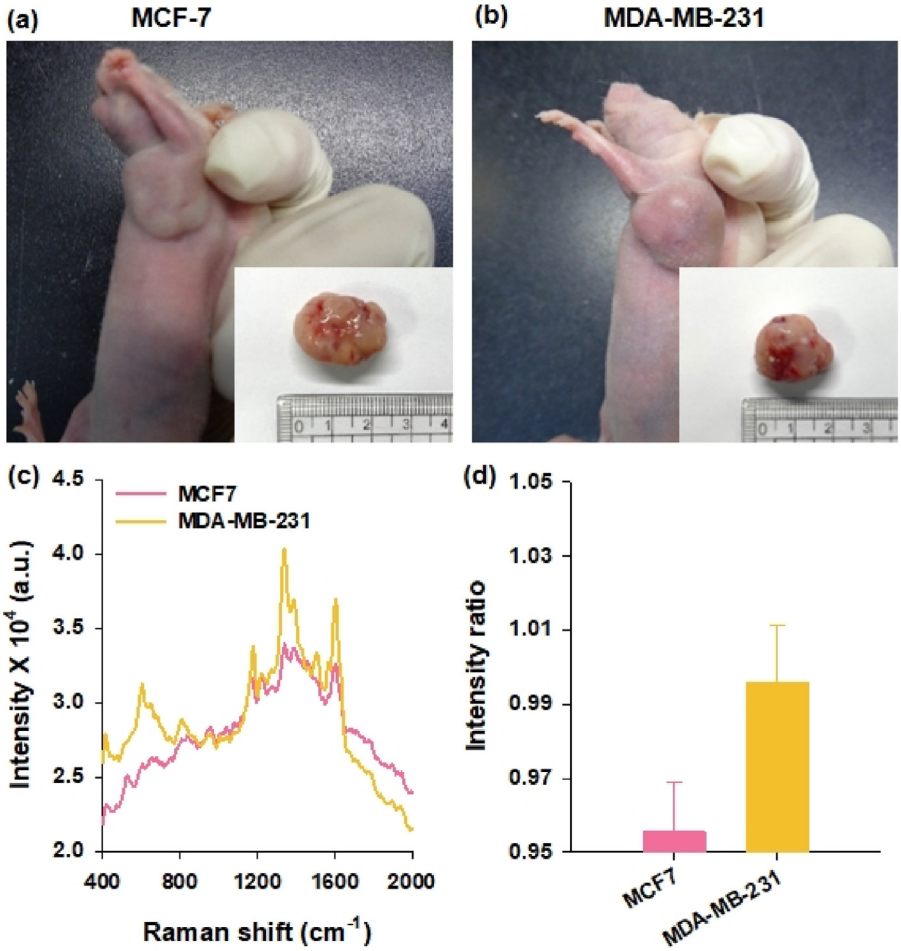


**Fig. 7.** Photographs of a) MCF-7 and b) MDA-MB-231 mouse models. c) Raman spectra and d) Raman intensity ratios of lysed cancer tissues extracted from MCF-7 and MDA-MB-231 mouse models.

## 4. Conclusion

In conclusion, we synthesized water-soluble Tween 80-coated polyaniline (TPAni) nanoparticles, which were successfully utilized as nanoagents for probing the redox activities of various cancer cells. The developed TPAni nanoparticles combined with the SERS analysis showed the improved sensing capability compared to the conventionally used absorbance ratio method. In addition, the silver nanosnowflakes (SNSF)-coated filter paper, SNSF-containing SERS substrate combined with TPAni nanoparticles was fabricated and applied to investigate the redox activities in different cancer cells originated from the same organ. Six different cancer cells from 3 different organs (MDA-MB-231 and MCF-7: breast, Huh-7 and SK-HEP-1: liver, A549 and H23: lung) were successfully analyzed, enabling to precisely identifying the correlation between their redox activities and aggressiveness. The potential of the developed method as an *in vivo* redox activity sensing platform was verified by successfully examining the lysed tumor samples extracted from breast cancer animal models. In the future, we will conduct research to investigate the cancer microenvironment by designing PAni nanoparticles that enables to measure specific biomarkers related to the microenvironment PAni nanoparticles to measure specific biomarkers for cancer microenvironment.

## Author contributions

Jahun Lee: Conceptualization, Methodology, and manuscript preparation. Hwunjae Lee: Methodology and manuscript preparation. Hyun Jung Kim: Methodology, Data curation, and manuscript preparation. Jongsu Yun: Methodology, Data curation, manuscript review and editing. Taeha Lee: Methodology and visualization. Gyudo Lee: Methodology and Data curation. Hyun Soo Kim: Supervision, Project administration, manuscript review, and editing. Yoochan Hong: Supervision, Project administration, manuscript review and editing.

## Data availability

The raw data required to reproduce these findings are available to download from [INSERT PERMANENT WEB LINK(s)]. The processed data required to reproduce these findings are available to download from [INSERT PERMANENT WEB LINK(s)].

## Declaration of competing interest

The authors declare that they have no known competing financial interests or personal relationships that could have appeared to influence the work reported in this paper.

## Acknowledgements

This study was funded by the project from Korea Institute of Machinery and Materials (KIMM) (NK232D, NK239E), the National Research Foundation of Korea grant supported by the Korean government (NRF-2018R1A6A1A03025242, NRF-2021R1C1C1012822, NRF-2021R1F1A1063455), and Research Resettlement Fund for the new

faculty of Kwangwoon University in 2021. This work was also supported by a Korea Medical Device Development Fund grant funded by the Korean government (Ministry of Science and ICT) (KMDF_PR_20200901_0264 and KMDF_PR_20200901_0127).

## Appendix A. Supplementary data

Supplementary data to this article can be found online at https://doi.org/10.1016/j.mtbio.2022.100241.

## References

[1] C.H. Foyer, M.H. Wilson, M.H. Wright, Redox regulation of cell proliferation: bioinformatics and redox proteomics approaches to identify redox-sensitive cell cycle regulators, Free Radic. Biol. Med. 122 (2018) 137–149, https://doi.org/10.1016/j.freeradbiomed.2018.03.047.

[2] D. Herrero, M. Tomé, S. Cañón, F.M. Cruz, R.M. Carmona, E. Fuster, E. Roche, A. Bernad, Redox-dependent BMI1 activity drives in vivo adult cardiac progenitor cell differentiation, Cell Death Differ 25 (2018) 809–822, https://doi.org/10.1038/s41418-017-0022-2.

[3] C.J. Dunnill, K. Ibraheem, A. Mohamed, J. Southgate, N.T. Georgopoulos, A redox state-dictated signalling pathway deciphers the malignant cell specificity of CD40-mediated apoptosis, Oncogene 36 (2017) 2515–2528, https://doi.org/10.1038/onc.2016.401.

[4] B. Singla, R. Holmdahl, G. Csanyi, Editorial: oxidants and redox signaling in inflammation, Front. Immunol. 10 (2019) 545. https://www.frontiersin.org/article/10.3389/fimmu.2019.00545.

[5] S. Messina, G. De Simone, P. Ascenzi, Cysteine-based regulation of redox-sensitive Ras small GTPases, Redox Biol 26 (2019) 101282, https://doi.org/10.1016/j.redox.2019.101282.

[6] R.A. Louzada, J. Bouviere, L.P. Matta, J.P. Werneck-de-Castro, C. Dupuy, D.P. Carvalho, R.S. Fortunato, Redox signaling in widespread health benefits of exercise, Antioxidants Redox Signal. 33 (2020) 745–760, https://doi.org/10.1089/ars.2019.7949.

[7] J.J. Serrano, B. Delgado, M.Á. Medina, Control of tumor angiogenesis and metastasis through modulation of cell redox state, Biochim. Biophys. Acta Rev. Canc 1873 (2020) 188352, https://doi.org/10.1016/j.bbcan.2020.188352.

[8] Q. Li, A. Wennborg, E. Aurell, E. Dekel, J.-Z. Zou, Y. Xu, S. Huang, I. Ernberg, Dynamics inside the cancer cell attractor reveal cell heterogeneity, limits of stability, and escape, Proc. Natl. Acad. Sci. 113 (2016) 2672–2677, https://doi.org/10.1073/pnas.1519210113.

[9] D. Pietraforte, W. Malorni, Focusing at the double-edged sword of redox imbalance: signals for cell survival or for cell death? Antioxidants Redox Signal. 21 (2014) 52–55, https://doi.org/10.1089/ars.2014.5914.

[10] R. Bakalova, Z. Zhelev, I. Aoki, T. Saga, Tissue redox activity as a hallmark of carcinogenesis: from early to terminal stages of cancer, Clin. Cancer Res. 19 (2013) 2503–2517, https://doi.org/10.1158/1078-0432.CCR-12-3726.

[11] E. Panieri, M.M. Santoro, ROS signaling and redox biology in endothelial cells, Cell. Mol. Life Sci. 72 (2015) 3281–3303, https://doi.org/10.1007/s00018-015-1928-9.

[12] C.A.R. Auchinvole, P. Richardson, C. McGuinnes, V. Mallikarjun, K. Donaldson, H. McNab, C.J. Campbell, Monitoring intracellular redox potential changes using SERS nanosensors, ACS Nano 6 (2012) 888–896, https://doi.org/10.1021/nn204397q.

[13] L.E. Jamieson, A. Jaworska, J. Jiang, M. Baranska, D.J. Harrison, C.J. Campbell, Simultaneous intracellular redox potential and pH measurements in live cells using SERS nanosensors, Analyst 140 (2015) 2330–2335, https://doi.org/10.1039/C4AN02365J.

[14] J. Choi, Y. Hong, E. Lee, M.-H. Kim, D.S. Yoon, J. Suh, Y. Huh, S. Haam, J. Yang, Redox-sensitive colorimetric polyaniline nanoprobes synthesized by a solvent-shift process, Nano Res 6 (2013) 356–364, https://doi.org/10.1007/s12274-013-0312-z.

[15] Y. Hong, S. Hwang, D. Heo, B. Kim, M. Ku, E. Lee, S. Haam, D.S. Yoon, J. Yang, J.-S. Suh, A magnetic polyaniline nanohybrid for MR imaging and redox sensing of cancer cells, Nanoscale 7 (2015) 1661–1666, https://doi.org/10.1039/C4NR06340F.

[16] Y. Hong, E. Lee, J. Choi, S. Haam, J.-S. Suh, J. Yang, Biomarker-specific conjugated nanopolyplexes for the active coloring of stem-like cancer cells, Nanotechnology 27 (2016) 225101, https://doi.org/10.1088/0957-4484/27/22/225101.

[17] Y. Cui, H. Chen, D. Tang, H. Yang, G. Chen, Au(iii)-promoted polyaniline gold nanospheres with electrocatalytic recycling of self-produced reactants for signal amplification, Chem. Commun. 48 (2012) 10307–10309, https://doi.org/10.1039/C2CC35351B.

[18] B. Zhang, Y. He, B. Liu, D. Tang, Nickel-functionalized reduced graphene oxide with polyaniline for non-enzymatic glucose sensing, Microchim. Acta 182 (2015) 625–631, https://doi.org/10.1007/s00604-014-1366-7.

[19] R. Zeng, Z. Luo, L. Zhang, D. Tang, Platinum nanozyme-catalyzed gas generation for pressure-based bioassay using polyaniline nanowires-functionalized graphene oxide framework, Anal. Chem. 90 (2018) 12299–12306, https://doi.org/10.1021/acs.analchem.8b03889.

[20] N. Kong, H. Zhang, C. Feng, C. Liu, Y. Xiao, X. Zhang, L. Mei, J.S. Kim, W. Tao, X. Ji, Arsenene-mediated multiple independently targeted reactive oxygen species burst for cancer therapy, Nat. Commun. 12 (2021) 4777, https://doi.org/10.1038/s41467-021-24961-5.

[21] X. Ji, L. Ge, C. Liu, Z. Tang, Y. Xiao, W. Chen, Z. Lei, W. Gao, S. Blake, D. De, B. Shi, X. Zeng, N. Kong, X. Zhang, W. Tao, Capturing functional two-dimensional nanosheets from sandwich-structure vermiculite for cancer theranostics, Nat. Commun. 12 (2021) 1124, https://doi.org/10.1038/s41467-021-21436-5.

[22] D. Gao, T. Chen, S. Chen, X. Ren, Y. Han, Y. Li, Y. Wang, X. Guo, H. Wang, X. Chen, M. Guo, Y.S. Zhang, G. Hong, X. Zhang, Z. Tian, Z. Yang, Targeting hypoxic tumors with hybrid nanobullets for oxygen-independent synergistic photothermal and thermodynamic therapy, Nano-Micro Lett. 13 (2021) 99, https://doi.org/10.1007/s40820-021-00616-4.

[23] T.F. Langford, B.K. Huang, J.B. Lim, S.J. Moon, H.D. Sikes, Monitoring the action of redox-directed cancer therapeutics using a human peroxiredoxin-2-based probe, Nat. Commun. 9 (2018) 3145, https://doi.org/10.1038/s41467-018-05557-y.

[24] S. Li, Z. Liu, C. Su, H. Chen, X. Fei, Z. Guo, Biological pH sensing based on the environmentally friendly Raman technique through a polyaniline probe, Anal. Bioanal. Chem. 409 (2017) 1387–1394, https://doi.org/10.1007/s00216-016-0063-2.

[25] H. Johnston, P. Dickinson, A. Ivens, A.H. Buck, R.D. Levine, F. Remacle, C.J. Campbell, Intracellular redox potential is correlated with miRNA expression in MCF7 cells under hypoxic conditions, Proc. Natl. Acad. Sci. 116 (2019) 19753–19759, https://doi.org/10.1073/pnas.1909455116.

[26] A.P. Silwal, H.P. Lu, Raman spectroscopy probing of redox states and mechanism of flavin coenzyme, J. Raman Spectrosc. 49 (2018) 1311–1322, https://doi.org/10.1002/jrs.5379.

[27] G. Kang, M. Yang, M.S. Mattei, G.C. Schatz, R.P. Van Duyne, In situ nanoscale redox mapping using tip-enhanced Raman spectroscopy, Nano Lett 19 (2019) 2106–2113, https://doi.org/10.1021/acs.nanolett.9b00313.

[28] Z. Chen, J. Liu, L. Tian, Q. Zhang, Y. Guan, L. Chen, G. Liu, H. Yu, Y. Tian, Q. Huang, Raman micro-spectroscopy monitoring of cytochrome c redox state in Candida utilis during cell death under low-temperature plasma-induced oxidative stress, Analyst 145 (2020) 3922–3930, https://doi.org/10.1039/D0AN00507J.

[29] W.J. Dong, J.Y. Han, X. Wu, L. Fan, W.T. Liang, A novel near-infrared fluorescence sensor for H2O2 based on N-Acetyl-L-Cysteine-Capped gold nanoparticles, J. Nano Res. 46 (2017) 234–240, https://doi.org/10.4028/www.scientific.net/JNanoR.46.234.

[30] Y.H. Lee, S. Jana, H. Lee, S.U. Lee, M.H. Lee, Rational design of time-resolved turn-on fluorescence sensors: exploiting delayed fluorescence for hydrogen peroxide sensing, Chem. Commun. 54 (2018) 12069–12072, https://doi.org/10.1039/C8CC07397J.

[31] X. Zhen, C. Zhang, C. Xie, Q. Miao, K.L. Lim, K. Pu, Intraparticle energy level alignment of semiconducting polymer nanoparticles to amplify chemiluminescence for ultrasensitive in vivo imaging of reactive oxygen species, ACS Nano 10 (2016) 6400–6409, https://doi.org/10.1021/acsnano.6b02908.

[32] L. Ruiyi, P. Tinling, C. Hongxia, S. Jinsong, L. Zaijun, Electrochemical detection of cancer cells in human blood using folic acid and glutamic acid-functionalized graphene quantum dot-palladium@gold as redox probe with excellent electrocatalytic activity and target recognition, Sensor. Actuator. B Chem. 309 (2020) 127709, https://doi.org/10.1016/j.snb.2020.127709.

[33] B. Lu, X. Yuan, Y. Ren, Q. Shi, S. Wang, J. Dong, Z. Nan, Cost-effective three dimensional Ag/polymer dyes/graphene-carbon spheres hybrids for high performance nonenzymatic sensor and its application in living cell H2O2 detection, Bioelectrochemistry 123 (2018) 103–111, https://doi.org/10.1016/j.bioelechem.2018.05.001.

[34] A. Garcia-Leis, I. Rivera-Arreba, S. Sanchez-Cortes, Morphological tuning of plasmonic silver nanostars by controlling the nanoparticle growth mechanism: application in the SERS detection of the amyloid marker Congo Red, Colloid. Surf. A Physicochem. Eng. Asp. 535 (2017) 49–60, https://doi.org/10.1016/j.colsurfa.2017.09.013.

[35] M. Lee, K. Oh, H.-K. Choi, S.G. Lee, H.J. Youn, H.L. Lee, D.H. Jeong, Subnanomolar sensitivity of filter paper-based SERS sensor for pesticide detection by hydrophobicity change of paper surface, ACS Sens. 3 (2018) 151–159, https://doi.org/10.1021/acssensors.7b00782.

[36] H. Soo Kim, T. Lee, J. Yun, G. Lee, Y. Hong, Cancer protein biomarker identification and quantification using nanoforest substrate and hand-held Raman spectrometer, Microchem. J. (2020) 105632, https://doi.org/10.1016/j.microc.2020.105632.

[37] S.H. Patil, A.P. Gaikwad, S.D. Sathaye, K.R. Patil, To form layer by layer composite film in view of its application as supercapacitor electrode by exploiting the techniques of thin films formation just around the corner, Electrochim. Acta 265 (2018) 556–568, https://doi.org/10.1016/j.electacta.2018.01.165.

[38] H.-J. Li, A.-Q. Zhang, Y. Hu, L. Sui, D.-J. Qian, M. Chen, Large-scale synthesis and self-organization of silver nanoparticles with Tween 80 as a reductant and stabilizer, Nanoscale Res. Lett. 7 (2012) 612, https://doi.org/10.1186/1556-276X-7-612.

[39] H. Lee, H.S. Kim, H.-W. Rho, Y.-M. Huh, Y. Hong, Multimodal cellular redox nanosensors based on self-doped polyaniline nanocomposites, J. Mater. Chem. B. 8 (2020) 10739–10743, https://doi.org/10.1039/D0TB02086A.

[40] F. Sotgia, U.E. Martinez-Outschoorn, S. Pavlides, A. Howell, R.G. Pestell, M.P. Lisanti, Understanding the Warburg effect and the prognostic value of stromal caveolin-1 as a marker of a lethal tumor microenvironment, Breast Cancer Res 13 (2011) 213, https://doi.org/10.1186/bcr2892.

[41] P. Breedveld, D. Pluim, G. Cipriani, F. Dahlhaus, M.A.J. van Eijndhoven, C.J.F. de Wolf, A. Kuil, J.H. Beijnen, G.L. Scheffer, G. Jansen, P. Borst, J.H.M. Schellens, The effect of low pH on breast cancer resistance protein (ABCG2)-Mediated transport of methotrexate, 7-hydroxymethotrexate, methotrexate diglutamate, folic acid, mitoxantrone, topotecan, and resveratrol in in vitro drug transport models, Mol. Pharmacol. 71 (2007) 240–249, https://doi.org/10.1124/mol.106.028167.

[42] P. Icard, S. Shulman, D. Farhat, J.-M. Steyaert, M. Alifano, H. Lincet, How the Warburg effect supports aggressiveness and drug resistance of cancer cells? Drug Resist. Updates 38 (2018) 1–11, https://doi.org/10.1016/j.drup.2018.03.001.